INTERNATIONAL JOURNAL OF INTEGRATED ENGINEERING
ISSN: 2229-838X e-ISSN: 2600-7916

IJIE

Vol. 16 No. 2 (2024) 348-362
https://publisher.uthm.edu.my/ojs/index.php/ijie

The Effect of Vibration on Flow Inside a Standing Wave Thermoacoustic Condition

Nur Afiqah Aina Zaiham[1], Fatimah Al Zahrah Mohd Saat[1,2]*, Yap Yu Xuan[1], Fadhilah Shikh Anuar[1,2], Patcharin Saechan[3]

[1] *Fakulti Teknologi dan Kejuruteraan Mekanikal (FTKM), Universiti Teknikal Malaysia Melaka (UTeM), Hang Tuah Jaya, 76100 Durian Tunggal, Melaka, MALAYSIA*
[2] *Green and Efficient Energy Technology (GrEET) Research Group, Centre for Advanced Research on Energy (CARe), Universiti Teknikal Malaysia Melaka (UTeM), Hang Tuah Jaya, 76100 Durian Tunggal, Melaka, MALAYSIA*
[3] *Department of Mechanical & Aerospace Engineering, Faculty of Engineering, King Mongkut's University of Technology North Bangkok, 1518 Pracharat 1 Rd., Bangsue, Bangkok, 10800, THAILAND*

*Corresponding Author: fatimah@utem.edu.my
DOI: https://doi.org/10.30880/ijie.2024.16.02.035

Article Info

Received: 17 May 2024
Accepted: 30 June 2024
Available online: 19 September 2024

Keywords

Thermoacoustic system, vibrating conditions, acoustic streaming, computational fluid dynamic (CFD), experimental study, ANSYS fluent

Abstract

This paper explores the complex relationship between acoustic streaming and vibration in thermoacoustic systems, enhancing the comprehension of these interconnected phenomena in the realm of energy conversion and heat transfer. Thermoacoustic devices are becoming more important for sustainable energy uses. The dynamic interaction between acoustic streaming and vibration is a crucial yet unexplored aspect of the performance of thermoacoustic devices. This research is driven by the necessity of filling current knowledge deficiencies and acknowledging the importance of these factors in the performance of thermoacoustic systems. This study intends to enhance the understanding about acoustic streaming and vibration through the utilisation of numerical simulations and experimental studies. In this paper, a two-dimensional (2D) computational fluid dynamics (CFD) model of standing wave thermoacoustic flow conditions was solved using the SST k-ω turbulence model in ANSYS Fluent to simulate the streaming induced by the vibrational responses within a standing wave thermoacoustic test rig. This numerical prediction is then validated using experimental results from a similar operating condition with a single resonance frequency of 23.6 Hz. Three drive ratios were examined. Disparity between velocity amplitude from CFD simulation and experimental data was observed particularly at the highest drive ratio. As the drive ratio increases, so does the amplitude of the velocity. It was discovered that the model that includes vibration brings the difference in results between the model and the experiment to be smaller and it replicates the closest scenario to the actual condition.

1. Introduction

Thermoacoustic systems transport energy through acoustic waves. An acoustic wave can generate an unsteady flow known as acoustic streaming [1]. Acoustic streaming is the secondary harmonic average flow caused by Reynolds stresses in a fluid that sustains an acoustic wave and is added to the primary acoustic wave [2], [3]. It

refers to the consistent fluid movement over time that occurs when acoustic waves travel through viscous fluids. Acoustic streaming is a significant nonlinear occurrence in the realm of physical acoustics [4]. It is often produced by the collision of an acoustic wave, such as a standing wave, with a solid wall [3]. Acoustic streaming effect has garnered significant attention and research due to its notable impact on dynamic flow, and disrupting boundary layer structure [2], [5]. Acoustic streaming is frequently identified as the cause of misinterpreted losses in thermoacoustic systems [6]. There have been numerous auditory streaming patterns that have been analyzed due to the varied methods of attenuation. These patterns have been analyzed in accordance with the diverse formation processes. Eckart streaming and boundary-driven streaming are two examples that stand out specifically [7], [8]. An Eckart streaming is a stable large-scale overall flow that exhibits vortex characteristics. This flow is created by the dissipation of energy that occurs when powerful sound waves propagate in free space [9]. The viscosity of the fluid medium is the primary factor that contributes to this phenomenon. In the meantime, boundary-driven streaming can be broken down into two categories: Schlichting streaming, which is also referred to as microflow [10], occurs in the boundary layer, and Rayleigh streaming, which begins within the boundary layer (inner streaming) and can extend into the fluid bulk (outer streaming) [4]. On the other hand, the Schlichting streaming that occurs in the acoustic boundary layer is typically not observable in most situations.

Rayleigh streaming is one of the several types of streaming, which derived from the viscous interaction that occurs between an acoustic wave and a solid boundary [11]. This paper primarily examines the impact of acoustic streaming on the thermoacoustic device, specifically in relation to the vibrating condition. Rayleigh streaming, which is caused by local mass and momentum variations induced by acoustic waves of the fluid flow within the thermoacoustic device, is a significant factor that can disrupt thermoacoustic flow patterns and impact on the effectiveness of thermoacoustic systems [12]. Consequently, it can be inferred that it will directly impact the workflows within the 'core' of the system where the 'stack' is located. The acoustic wave's interactions with fluid phenomena in the thermoacoustic rig disturb the symmetrical distribution of the acoustic streaming structure. Furthermore, it has been noted that the acoustic streaming intensity increases proportionally with the amplification of energy input into the system [7]. When the fluid flow encounters the solid wall and there is a phase difference between the pressure and motion, the fluid behavior will experience acoustic streaming and disturbance in the boundary layer [13] as it moves back and forth. This leads to the introduction of non-linear effects in thermoacoustic devices [4]. Nevertheless, this can result in variations in pressure [14]. Consequently, typical means of reducing energy loss may not be enough to decrease the intensity of the combined pressure waves, resulting in the intensification of pressure waves, which are referred to as thermoacoustic vibrations. In general, vibrations have had a significant impact on the regular functioning of the system, leading to considerable noise and possibly structural harm [15]. According to the study conducted by [14]'s work in 2019, vibrations can have negative effects on thermal efficiency, leading to affecting the flow patterns caused by acoustic streaming. The interplay between vibrations and acoustic waves can modify the strength and orientation of streaming flows, which in turn impacts the circulation of fluids, heat transfer processes, and overall functioning of thermoacoustic systems [16].

Numerous experimental and theoretical approaches have been investigated to gain a deeper understanding and mitigate acoustic streaming. A numerical simulation was performed by Yang et al. [7] to investigate the combined of temperature and fluid flow interaction to change the control equations for partial differential of acoustic streaming in a designed model. A temperature gradient acting in different directions has a substantial impact on the flow structure distortion. To numerically solve the Navier-Stokes equations, Aktas and Farouk [17] utilized a computational fluid dynamics (CFD) method. Their aim was to study how acoustic streaming patterns in a 2D rectangular model are affected by the strength of the acoustic field. Researchers have shown that acoustic streaming becomes progressively distorted as the acoustic field strength rises. These structures acoustic streaming structure are primarily caused by the fluid inertia that effect from a strong acoustic wave. Mahdaoui et. al. [1] use CFD for foreseeing acoustic streaming in complex geometries and at increased pressure drive ratios, as well as the related non-linear streaming phenomena. The analysis revealed that the chosen model does not accurately account for the highly nonlinear streaming occurring inside the system. Nevertheless, the research conducted by Nouh et al. [18] observed the existence of mechanical vibration in the thermoacoustic system while it undergoes the conversion process within the resonator. The research primarily concentrated on utilizing dynamic magnification to enhance the intensity of the vibrations.

To some extent, previous studies have successfully demonstrated the correlation between simulation and experimental measurements, as well as providing the understanding of acoustic streaming phenomena which primarily describe the changes of acoustic streaming patterns caused by geometry model, acoustic intensity, and temperature field. However, there is a lack of comprehensive investigations into the characteristics of the acoustic streaming field under the influence of the thermoacoustic physical field such as vibration. Nevertheless, the influence of vibration on acoustic streaming is frequently disregarded. Although several research have observed the existence of thermoacoustic vibration, the correlation between vibrating condition and acoustic streaming, as well as their impact on the acoustic wave within the porous structure, has been investigated separately. The acoustic wave in the thermoacoustic system is influenced by thermoacoustic vibration and streaming, which in

Int. Journal of Integrated Engineering Vol. 16 No. 2 (2024) p. 348-362

turn cause nonlinearity in the compression and expansion conditions [18]. Therefore, vibrations have a substantial impact on the streaming flow, as they affect the entire cycle in a thermoacoustic system. Due to the substantial amount of literature on acoustic streaming in general and the scarcity of combined research on acoustic streaming and vibrating condition in thermoacoustic devices, it is necessary to thoroughly study the correlation between these two parameters. In this paper, an insight into the impact of vibration on thermoacoustic flow conditions is presented with an operating condition that is kept at a constant room temperature. The effect of temperature on the flow was excluded so that focus can be given on the impact of Rayleigh streaming on thermoacoustic flow [19]. Focusing all parameters all at once may not be a reliable option due to difficulty in identifying the contributing factors for the investigated phenomena. The explanation of experimental setup and numerical works is included in Section 2. Section 3 presents a comparison of the numerical results with both experimental and theoretical data to validate the model. The findings of the flow velocity and vibration effect from the experimental works will be discussed further through numerical works for both the cases: with and without vibrating circumstances, are presented in Section 3.

2. Methodology

In this section, the methodology for both experimental and computational fluid dynamics (CFD) works are described. The investigation of flow velocity and vibration conditions on flow streaming at three different drive ratios over the 'stack' of the thermoacoustic system is carried out. In this study, the experimental data and theoretical calculation were used to validate the 2D CFD models.

2.1 Experimental Works

The experiments were conducted using a thermoacoustic rig equipped with a quarter wavelength setup, in which the resonator was arranged to be at approximately a length of 0.25λ. The wavelength, denoted as λ, can be determined using Equation (1). It is important to note that the speed of sound, represented as c, was assumed to remain constant at room temperature during this computation. The selection of this quarter-wavelength resonator was based on its lower resonator wall losses in comparison to longer resonators [20].

$$\lambda = \frac{c}{f} \tag{1}$$

Fig. 1 depicts the thermoacoustic rig and the schematic diagram of the experimental apparatus setup, including measurement devices, a loudspeaker as an acoustic driver, a resonator, and a parallel-plate structure referred to as a 'stack' positioned inside a test section at a specific location of 0.17λ from the rigid end of the resonator. The selection of this location is based on the thermoacoustic impact, as documented in the research conducted by Mohd Saat and Jaworski. This study involves a thermoacoustic flow at a single resonance frequency, f of 23.6 Hz. This frequency is associated with a resonator tube that has a length of 3.8 meters and a cross-sectional area of 150 mm x 150 mm. In this thermoacoustic test system, the resonator is typically constructed with a flow route for air to facilitate operation at the resonance frequency, hence maximizing performance. To avoid too many interfering factors so that focus can be given on the main flow, the apparatus lacks the necessity of heat exchangers. The pores themselves retain the heat flow, which is then utilized as a heat source in the subsequent cycle [22], [23].

At a pressure antinode (x = 3.8m), a 700W subwoofer type 18-inch diameter loudspeaker (Precision Device 1860) is attached to the resonator tube via a converging channel [20]. It is noteworthy that the pressure antinode represents the point at which the amplitude of the acoustic wave's pressure is at its peak. The current study utilizes a resonator with a pressure antinode situated at its most rigid point. The designation for this location is P_a in Fig. 1. To ensure the resonator was securely connected and to prevent air loss from the apparatus, the connections were sealed with rubber mat. A power amplifier (Fletcher FLP-MT1201) and a function generator (SG1005) are utilized to energize the speaker's input. The flow of current is adjusted in accordance with the peak-to-peak voltage supply, Vpp, and frequency. To generate an oscillatory flow, a sinusoidal wave is directed from the function generator to the speaker [23]. The amplitude of flow velocity in thermoacoustic oscillatory flow is dependent on the variation in the peak-to-peak voltage supply. At the pressure antinode location, a piezoresistive pressure sensor (Endevco 8510B) is fixed to the closed end of the resonator (defined as x = 0). Its purpose is to capture the pressure amplitude value. In the context of a quarter wavelength resonator, the pressure theoretically reaches its maximum at the pressure antinode. Therefore, this site serves as the standard against which the amplitude of oscillatory flow in thermoacoustic is measured.

The plates were chosen for their homogenous porosity structure [24], [25], which consists of a uniform parallel arrangement. This configuration was selected due to its ease of maintenance and manufacture [20]. The parallel plates demonstrate a 'stack' composed of twelve aluminum plates. Each plate has a length (l) of 200 mm, a thickness (d) of 3 mm, and is separated from the adjacent plate by a distance (D) of 6 mm. In the field of

thermoacoustics, the term 'stack' refers to a significant solid surface known as the 'core' of the system. This is where the thermodynamic processes of the energy system occur [22], [26], [27], [28]. The configuration of a 'stack' results in a porosity of 76.66%. Porosity is defined as the proportion of the stack's volume that is filled with air, relative to the total volume of the 'stack'.

(a)

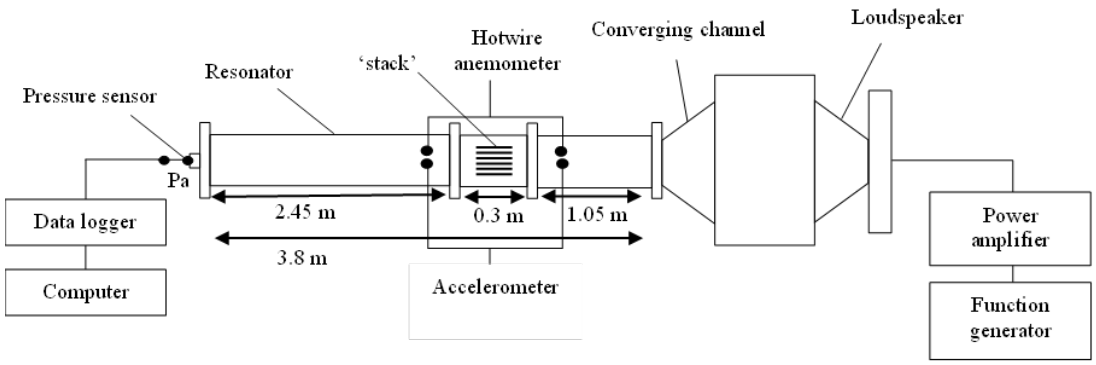

(b)

Fig. 1 *(a) Real picture of thermoacoustic rig; (b) Schematic diagram of 23.6 Hz rig*

In this study, the velocity amplitude of the flow was determined by employing a hotwire anemometer (ST-732). The hot wire probe was positioned at approximately 120 mm from the 'stack', between its two ends. The investigation involved measuring the amplitude velocity of the flow at specific points labelled as *v*1 and *v*2 within the resonator. These locations are indicated in Fig. 2. Furthermore, it is anticipated that vibrations occurring along the resonator and converging channel will generate potential vibration during the experimental work. This parameter should be prioritized as it is often overlooked by many researchers, even though vibrations at certain locations of the axis can have a relatively impact on the resonator body. Therefore, it is necessary to investigate this parameter to determine its influence on the streaming and flow velocity within the thermoacoustic system. An accelerometer (specifically the SDL-800 model) was positioned on both axes of the resonator body and converging channel to gauge the vibration levels that could potentially enhance the flow of streaming. The vibration of the resonator and oscillations of the system were measured in terms of displacement along the *y* and *z* axes to determine the potential vibrations experienced [29]. The location of vibrations measured along two axes is also illustrated in Fig. 2.

The experimental data on velocity amplitude and vibrations were utilized to validate the models employed in the study. The validation of numerical model with experimental results is essential to demonstrate the efficacy of the modelling approach and verify that the simulations accurately depict the physical environment in experimental work. The dashed box in Fig. 2 denotes the specific region inside the computational domain that will be addressed in the subsequent subsection.

The flow within the resonator tube is allowed to continue running for five minutes prior to the begin of data collection. The purpose of this is to maintain a consistent and stable environment within the resonator. The experiments were replicated three times, with each data point being captured for an approximate duration of two minutes. This was conducted as a part of the uncertainty analysis to estimate the repeatability and accuracy of the results. Equation (2) represents the general formula for determining the average value of data, denoted as $\bar{x}$.

$$\bar{x} = \frac{1}{n}\left(x1 + x2 + \cdots + xn\right) \tag{2}$$

Int. Journal of Integrated Engineering Vol. 16 No. 2 (2024) p. 348-362

where *n* represents the frequency of the measurement. The value of *n* in this study is 3, as the experiments were repeated three times. The deviation from the mean is utilized to calculate the experimental error. Equation (3) provides the definition of the standard deviation, denoted as *s*, which is the parameter used to assess the accuracy of the data collected for the study [23]. Utilizing this analytical approach is crucial in order to guarantee the replicability and dependability of the data obtained.

$$s = \sqrt{\frac{1}{(n-1)}[\,(x_1 - \bar{x})^2 + \cdots + (xn - \bar{x})^2]} \tag{3}$$

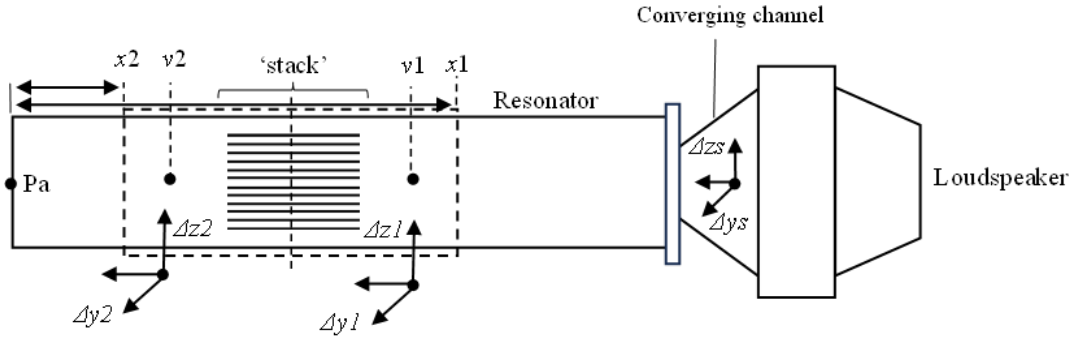

Fig. 2 *Schematic diagram of a quarter wavelength thermoacoustic system with a dashed box that represents the location of the computational domain*

2.2 Numerical Works

To analyze the fluid flow and vibrating conditions numerically, computational fluid dynamics (CFD) models were applied, which were based on the experimental setup used earlier in this study. This work primarily utilized ANSYS Fluent, a computational tool employed for simulating fluid flow [30]. The element quality and skewness are assessed to ensure they remain within specified ranges. The domain was simulated using a two-dimensional (2D) computational fluid dynamics (CFD) model because of its computational efficiency [31] compared to three-dimensional (3D) modelling, which would need significantly more time and computer resources [32]. The simplification of the 2D model is expected to be feasible and solvable, as it is anticipated that there will be no significant alterations in the parameters or properties of the 3D model [32]. The computational domain utilized in this investigation, as seen by the dashed box in Fig. **2**, encompasses a rectangular region measuring 1000 mm in length and 142 mm in height surrounding the test portion. The determination of the domain's length is derived from the recommendation provided by [33] as cited in the study conducted by [34]. It is advised that the domain's length should neither be excessively brief nor excessively long.

Fig. 3(a), (b) and (c) displayed the geometry of the model with specified boundary conditions from the dash-box in Fig. **2**, meshing geometry of the computational domain, and an enlarged view of mesh generation near the parallel-plate and wall, respectively. The computational domain shown in Fig. 3(b) illustrates the standing wave thermoacoustic system with the 'stack' positioned at the center of the domain. The Shear-Stress Transport (SST) k-ω turbulence model were used in solving the 2D CFD model as it has been demonstrated to effectively represent the fluid dynamics of flow around the boundary layer of the thermoacoustic system [21], [34]. This model has demonstrated outstanding performance even in scenarios with adverse pressure gradients, such as those encountered in cyclic flow conditions of thermoacoustic.

The quadrilateral mesh was created with a growth rate of 1.2. The domain was splitted into regions, with each parts having a structured mesh to minimize skewness and achieve higher mesh quality [35] for the domain, primarily when the bias setting is applied [37]. A more complex mesh was implemented within the region near the parallel-plate structure to accurately depict the fluid flow variations in those specific areas [36] . Meanwhile, a smaller mesh was created along the top and bottom walls of the domain, as depicted in Fig. 3(c), to accommodate the vertical movements of the domain when the moving wall is applied. The bias setting can be used to apply a finer and more compact mesh to the domain. The mesh underwent grid independence testing, which determined that a total grid number of 58396 is adequate for obtaining results that are not influenced by the grid size. This corresponds to a y^+ (y-plus) value of 0.89, which was recommended as the appropriate number for fine grid near-wall mesh refinement in order to generate the viscous sub-layer [37]. The mesh has a minimum orthogonal quality of 0.99 and a maximum skewness of 8.829 x 10^{-3}, indicating that it is in a state of good quality.

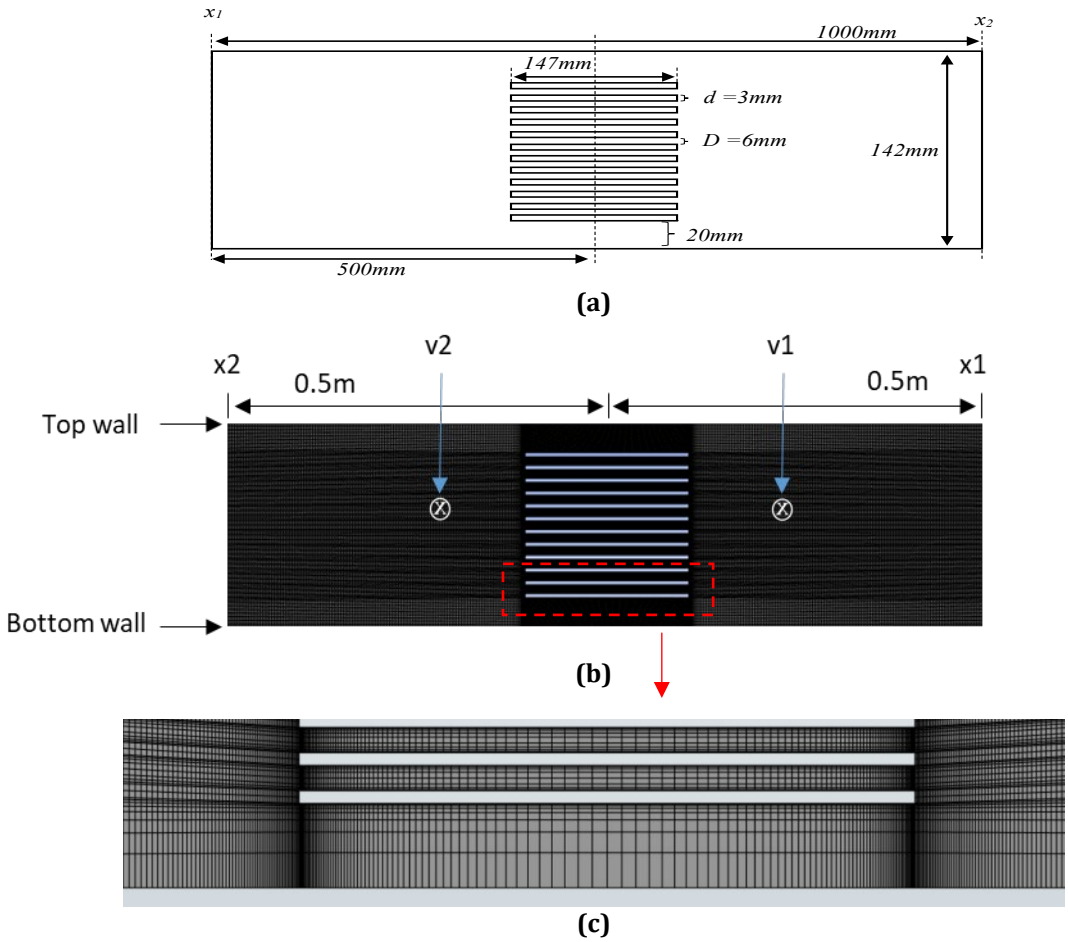

Fig. 3 *(a) 2D geometry of the model; (b) Meshing of computational domain; (c) Enlarge view of mesh generation near the parallel-plate area and wall*

The model was solved for various flow amplitudes, which are quantified by a term called as drive ratio, DR, as indicated in Equation (4). The drive ratio is defined as the ratio between the acoustic pressure at the position of the pressure antinode, P_a, and the mean pressure, P_m. The mean pressure corresponds to the air pressure within the resonator. The ideal gas equation was selected to model the variations in density of the working fluid, air, under atmospheric pressure conditions. The mean pressure, P_m, is equal to 100 kPa while the mean air temperature, T_m, is 300K. The oscillatory flow behavior at the inlet, outlet, top, and bottom walls of the domain shown in Fig. 3(b) were generated using user-defined-function (UDF) codes. An oscillating pressure, labelled as P_1, was designated as the inlet condition at the x_1 position of the domain. The outlet boundary at the x_2 position of the domain was characterized by an oscillating velocity, designated as U_2. The oscillating velocity at the top and bottom walls of the domain, referred to as U_w, was initially described as a non-moving wall for the purpose of validating it against earlier work. It was later redefined as a moving wall. The inlet, outlet, top, and bottom wall conditions are determined using lossless equations, as depicted in Equations (5), (6), and (7).

$$\boldsymbol{DR = \frac{P_a}{P_m}} \tag{4}$$

$$\boldsymbol{P_1 = P_a\, cos\,(k_a X_1)\, cos(2\pi f t)} \tag{5}$$

$$\boldsymbol{U_2 = \frac{P_a}{pc}\, sin(k_a X_2)\, cos(2\pi f t + \theta)} \tag{6}$$

$$\boldsymbol{U_w = 2\pi f\, x\, \Delta\, cos(2\pi f t)} \tag{7}$$

$$\boldsymbol{k_a = \frac{2\pi f}{c}} \tag{8}$$

Int. Journal of Integrated Engineering Vol. 16 No. 2 (2024) p. 348-362

where k_a, P_a, f, t, c, θ, Δ, x_1, and x_2 represent the wavenumber, acoustic pressure at the position of pressure antinode, flow frequency in Hz, time, speed of sound, phase at 90 degrees in radians, displacement of vibrations along the y or z axis, and the locations of the inlet and outlet of the domain, respectively. The wave number, k_a, is determined by the angular velocity (ω) and is mathematically specified in Equation (8). Two supplementary boundary conditions were computed and considered, the turbulent length scale, denoted as $\ell = 0.07\ D$, and the turbulent intensity, represented by $TI = 0.16\ (\mathrm{Re})^{-1/8}$. The diameter, denoted as D, of the turbulent length scale is determined by the height of the resonator. The Reynolds number used to calculate turbulence intensity [38] was determined by the theoretical velocity amplitude at the respective boundary location following the practice reported in published work [40].

Table 1 *Boundary condition for non-moving wall and moving wall*

Boundary names	Non-moving wall case	Moving wall case
Inlet	Pressure inlet (i.e., Eq. (5))	Pressure inlet (i.e., Eq. (5))
Outlet	Velocity outlet (i.e., Eq. (6))	Velocity outlet (i.e., Eq. (6))
Top and Bottom walls	Stationary wall	Moving wall (i.e., Eq. (7))

The models were solved using an unsteady pressure-based implicit solver, specifically employing the Pressure-Implicit with Splitting Operators (PISO) technique for the pressure-velocity coupling. The PISO approach is renowned for its stability and computing efficiency. It successfully handles pressure-velocity interactions, allowing for precise prediction of fluid flow behavior [39]. The SST k-ω turbulence model was computed using the Reynolds-Averaged-Navier-Stokes (RANS) equation [40] provided by ANSYS Fluent. The model utilizes the principles of mass, momentum conservation, and total energy equation, as specified in Equations (8) to (10). The transient model was implemented using a time step size of $1/1000\ f$. Convergence was obtained between 10 and 20 iterations for each time step. The models were iterated for a minimum of six cycles each. The purpose of this is to provide a consistent oscillatory flow condition in which the thermodynamic characteristics of the flow remain constant from one cycle to the next.

$$\frac{\partial \rho}{\partial t} + \nabla.(\rho u) = 0 \tag{8}$$

$$\frac{\partial \rho u}{\partial t} + \nabla.(\rho u u) = -\nabla \mathrm{p} + \nabla.\tau + \mathrm{F} \tag{9}$$

$$\frac{\partial}{\partial t}\left[\rho\left(e + \frac{1}{2}u^2\right)\right] + \nabla.\left[\rho u\left(e + \frac{1}{2}u^2\right)\right] = \nabla.(\mathrm{k}\nabla \mathrm{T}) + \nabla.(-\mathrm{pu} + \tau.\mathrm{u}) + \mathrm{u}.\mathrm{F} + \mathrm{Q} \tag{10}$$

The terms ρ, u, t, p, τ, F, e, k, and Q represent the density, velocity, time, pressure, shear stress components, body force, enthalpy, thermal conductivity and heat, respectively.

3. Results and Discussion

This section begins with the outcomes of model validation. Subsequently, the verified models are utilized to generate outcomes related to the amplitude of velocity and the condition of vibration along the thermoacoustic rig. The results indicate that thermoacoustic vibrations have a substantial influence on the fluid dynamics of oscillatory flow within a thermoacoustic system.

3.1 Model Validation and Verification

In order to validate the 2D CFD model, the results of velocity amplitude were compared with both experimental data and theoretical calculations. The drive ratio values used for comparison were 0.64%, 2.17%, and 3.01%, as specified in the experimental works. The comparisons were conducted at the same location, specifically 120 mm from the end of the 'stack', and with the same porosity value. To validate the data, the location for data collection was carefully selected to minimize potential mistakes caused by flow disturbances near the parallel-plate structure. The porosity is determined by dividing the cross-sectional area of the plates in the 'stack' by the cross-sectional area of the resonator. The axial velocity amplitude was measured both theoretically and experimentally at this position with 100% porosity. Dimensionless values were calculated using reference velocity. The reference velocity, V_{ref}, was calculated based on the inlet boundary condition of the computational domain. The value varies based on the drive ratio. Table 2 shows the V_{ref} values for all drive ratios examined in this study. The equation used to calculate the V_{ref} is displayed in Equation (11).

Table 2 *Velocity reference, V_{ref} for investigated drive ratios at porosity 100%*

Drive ratio %	Velocity reference, V_{ref}
0.64	1.2061
2.17	4.0704
3.01	5.6554

$$\boldsymbol{V_{ref} = \frac{k_a P_a}{\phi\, \omega\, \rho} \sin(k_a\, x)} \quad (\mathbf{11})$$

The variables k_a, P_a, ϕ, ω, and ρ represent the wavenumber, pressure amplitude at the position of pressure antinode, porosity at the location of data measured, the angular velocity, and the density of the fluid, respectively. The x location refers to the specific location where the data for validation was collected.

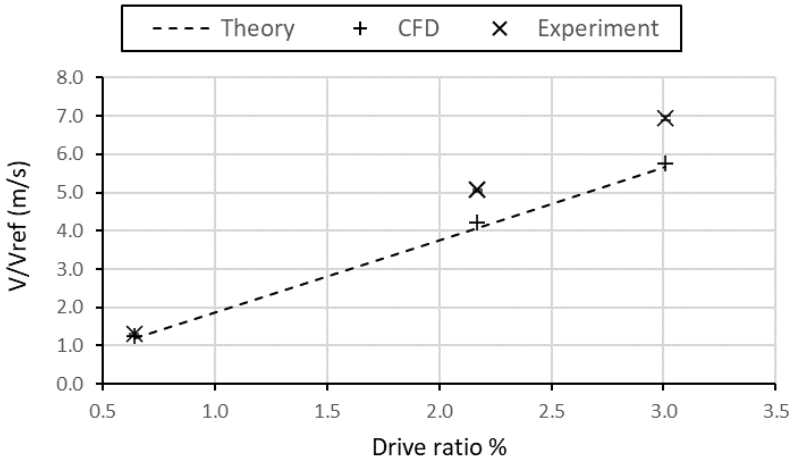

Fig. 4 *Validation of the model with theoretical calculations and experimental results*

The changes in velocity amplitude with respect to drive ratio were illustrated in Fig. 4, which allows for validation of the results obtained from experimental measurements, CFD simulation, and theoretical calculation. The outcomes of the CFD simulation approach the theoretical values more closely, particularly when considering the minimum drive ratio of 0.64%. The CFD outcomes exhibit small changes in comparison to the theoretical values, with a comparatively lesser deviation of 1.93% observed at the maximum drive ratio of 3.01%. In contrast, the experimental data exhibit significant differences from the linear theory's calculations, with the greatest differences of 19% occurring at the maximum drive ratio of 3.01%. Error bars in Fig. 4 illustrated the accuracy of the experimental data, serving to denote the uncertainties associated with the values obtained. The uncertainties associated with the data collection in Equation (3) were computed utilizing the standard deviation method. Evidently, the differences between the experimental values and those measured through CFD simulation and theoretical formulas are clearly observed. The differences become more apparent when the drive ratio is increased to 3.01%, a similar trend that was also mentioned in the earlier published work [41]. The huge difference shown between CFD simulation and experimental data is approximately 17%.

Notably, the deviation may have been caused by a perceptible vibration that occurred along the thermoacoustic rig during the experimental work, thereby disrupting the fluid flows within that area. This vibration may result in additional streaming within the apparatus, which may introduce an error to the measured velocity value. Potential efforts were made to ensure that data could be collected throughout an extensive range of flow amplitudes in order to validate the numerical model. The rig was meticulously mounted to the table by affixing rubber gaskets to multiple joints to mitigate vibration concerns. Regrettably, when the drive ratio is increased, the intensity of vibrations in the experimental rig also increases, making it impossible to obtain accurate velocity data. However, the current model's observing of a comparable relationship between velocity change and drive ratio and magnitude, which aligns with experimental and theoretical calculations, offers valuable insights into the fluid dynamics of flow within the thermoacoustic rig. Therefore, the models still provide valuable insights into the fluid dynamics within the system under optimum circumstances but the noticeable vibration during experimentation requires special attention, especially at high drive ratio condition.

Int. Journal of Integrated Engineering Vol. 16 No. 2 (2024) p. 348-362

3.2 Velocity Amplitude

As outlined in the experimental setup methodology, the experiments were conducted using a quarter-wavelength thermoacoustic rig, corresponding to a frequency of 23.6Hz. The experiment was carried out with a loudspeaker operating within the provided range of peak-to-peak voltage, Vpp, from 0.05 V to 0.50 V. Meanwhile, the numerical simulation was done using the validated 2D CFD model in ANSYS Fluent, following the methodology outlined in this study. The velocity amplitude range of flow in experimental and numerical works was first verified through theoretical calculations. The velocity amplitude results for CFD and experimental works at location 2 can be seen in Fig. 5. The data is provided for three different drive ratios: 0.64%, 2.17%, and 3.01%. The measured amplitude velocity for both experimental and numerical works can be found in Fig. 2, located approximately 120 mm from the end of the 'stack'. This location has been identified as the central point within the resonator, offering valuable insights into the acoustic streaming behavior during the compression and expansion process in the thermoacoustic rig.

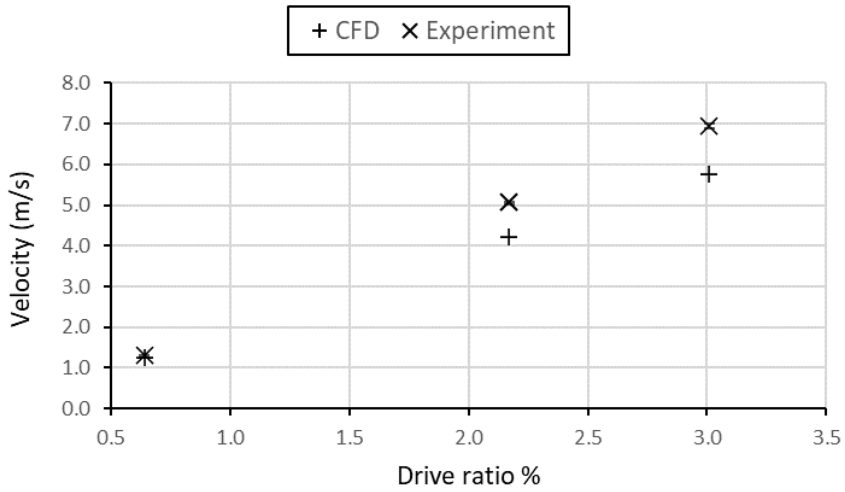

Fig. 5 *Comparison between CFD simulation and experimental results*

The correlation between these two data is readily apparent, as the drive ratio increases, the velocity amplitude increases as well. The relationship between drive ratio and velocity amplitude in thermoacoustic systems is primarily determined by the interaction between acoustic waves and the mechanical vibrations of the system. Increasing the drive ratio can result in amplified sound waves that propagate through the resonator, thus enhancing the velocity amplitude within the thermoacoustic system [12]. The CFD modelling and experimental studies demonstrate a favorable agreement with a minor difference of 5% for the low drive ratio. The velocity amplitude results are then increased when the drive ratio reaches 2.17%. The huge difference between CFD and numerical results indicates that both are 16.6% different from one other. According to both CFD and experimental studies, the experimental results differ from the CFD results by 17% at a drive ratio of 3.01%. The differences between CFD and practical results at high drive ratio can be attributed to the mechanical vibrations of the thermoacoustic rig, which affect the acoustic streaming within the resonator. The mechanical vibrations of the thermoacoustic rig can amplify the amplitude of the acoustic waves, resulting in increased velocity amplitudes in the flow of the working medium (i.e. air). Therefore, the presence of mechanical vibration throughout the experimental work has been identified and acknowledged as the primary factor contributing to the discrepancies with the results obtained from computational fluid dynamics (CFD). Extensive research has been conducted to investigate the vibrating condition, both experimentally and numerically. The focus of the numerical studies has been on accurately modelling the vibration to closely resemble actual situations observed in the experimental environment. This topic will be further discussed in the following subsection.

3.3 Vibration Condition

3.3.1 Experimental Results

Thermoacoustic devices frequently exhibit natural frequencies at which they resonate during the experimental work. When the acoustic waves are driven by an acoustic driver (i.e. loudspeaker), the frequency produced by the system matches its natural frequency, resonance evolves, resulting in increased vibrations [42]. The vibrating circumstances that occurred throughout the experimental work were recorded on the thermoacoustic rig. This

condition was clearly identified throughout the experimental work, particularly when the thermoacoustic system was subjected to high peak-to-peak voltage supply, Vpp for the acoustic driver.

Table 3 *Vibration at the thermoacoustic rig for Z and Y axes at points 1 and 2*

Vpp (V)	Displacement (x10^{-4}) m			
	ΔZ1	ΔZ2	ΔY1	ΔY2
0.05	0.213	0.187	0.010	0.007
0.10	0.410	0.363	0.167	0.010
0.15	0.583	0.533	0.030	0.020
0.20	0.743	0.678	0.030	0.020
0.25	0.887	0.810	0.033	0.030
0.30	0.990	0.923	0.047	0.033
0.35	1.100	1.033	0.050	0.037
0.40	1.197	1.103	0.057	0.040
0.45	1.290	1.203	0.063	0.047
0.50	1.360	1.293	0.070	0.060

The detailed arrangement of the experimental setup can be found in Fig. 1(a). The vibration was recorded using an accelerometer at several locations along the resonator. The accelerometer sensor is strategically placed on the resonator body to accurately measure displacement in two directions. Vibrations were recorded at both the *Y* (horizontal) and *Z* (vertical) axes at the location of points 1 and 2, which were approximately 120 mm from both ends of the 'stack', same as the location where velocity amplitude were measured. This allows the vibration conditions to be captured at same dynamic behavior as velocity amplitude when the acoustic streaming interacts with the solid wall of the resonator body. Location of point 1 refers to the position nearest to the speaker that is attached to the thermoacoustic rig. Point 2 is positioned at the location nearest to the pressure antinode at the rigid end of the resonator. Given the constraints of the loudspeaker's capabilities, the experiments were conducted within the voltage range of 0.05V to 0.50V of Vpp. According to Table 3, the vibration levels rose for both axes as the provided Vpp increased. It is important to mention that increasing the voltage supplied to the system results in a greater amount of input energy, which in turn leads to more intense acoustic waves. However, it is noticed that the measured data on the Y-axis have a lower order of magnitude compared to the measured data on the Z-axis. It was discovered that excitation of the resonator body is causing bigger vibrations along the Z-axis. There is an excessively small amount of vibration on the Y axis, and it appears to be practically stable. This vibration data shows when Vpp values range from 0.15V to 0.25V for location point 1, as well as for location point 2. Due to this concern, it is anticipated that the vibration along the Y-axis is not significant enough to have a substantial impact on the acoustic streaming of fluid flow, and hence it is not worth considering. Therefore, the vibration along this axis appears to be neglected in this study. The vibration on Z-axis is large, which is expected the vibration on this axis can be considered in influencing the acoustic streaming inside the resonator body. Thus, the investigation of vibration condition in this study will be more focused on the Z-axis.

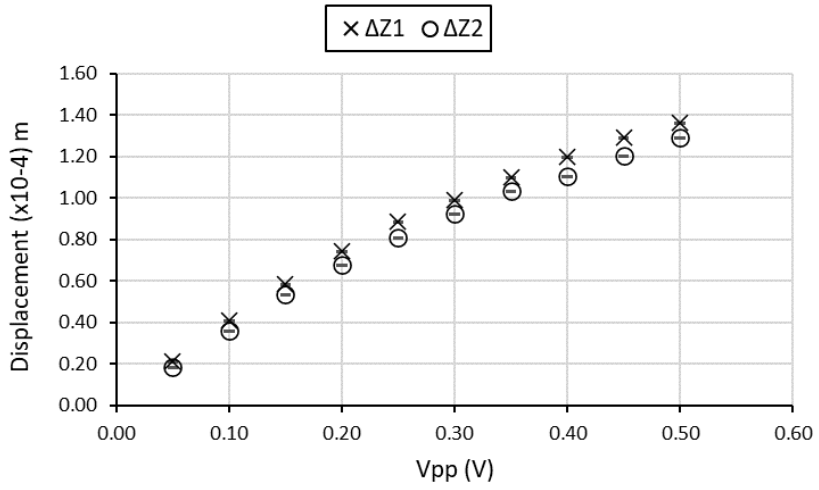

Fig. 6 *Comparison of vibration data for Z-axis*

Int. Journal of Integrated Engineering Vol. 16 No. 2 (2024) p. 348-362

According to Fig. 6, the vibration data at ΔZ1 are slightly higher than the vibration levels recorded at ΔZ2. The measured vibration is influenced by its location. As previously stated, the vibration of ΔZ1 was observed at location point 1, which is close to the acoustic driver. Therefore, it is anticipated that the driver may encounter stronger acoustic streaming effects, resulting in increased vibrations in that area. Meanwhile, the vibration of ΔZ2, which was recorded near the pressure antinode, suggests lower vibration data. This phenomenon occurs when acoustic waves propagate through the thermoacoustic system in a cyclical manner, repeatedly traveling back and forth across a structure known as 'stack'. The 'stack' itself can attenuate a certain amount of the acoustic energy because of the thermoacoustic process. Hence, the acoustic waves generally undergo attenuation [43]. As the waves travel further away from the acoustic driver, they experience greater attenuation. This situation is subject to causing a decrease in their intensity and consequently, decreased the vibrations. However, the vibration patterns for both locations exhibit a strong consistency, with the maximum difference between them being around 12%. Instead of solely focusing on the resonator part, an alternative approach to investigating the existence of vibration lies in the converging channel (also known as the cone) that is attached to the acoustic driver. As previously stated, the proximity of the thermoacoustic part to the acoustic driver will result in increased vibrations in that specific area.

Table 4 *Vibration at the converging channel for Z and Y axes*

Vpp (V)	Displacement (x10^{-4}) m	
	ΔZs	ΔYs
0.05	0.227	2.183
0.10	0.467	4.463
0.15	0.687	7.193
0.20	0.897	10.260
0.25	1.043	12.417
0.30	1.157	14.233
0.35	1.280	15.343
0.40	1.447	16.187
0.45	1.553	17.113
0.50	1.633	18.550

The location of the measured point within the converging channel was as shown in Fig. 2. Based on Table 4, for the location of axes, the vibration fluctuated higher, especially on the Y-axis. The converging channel is positioned near the acoustic driver in order to effectively propagate the acoustic waves. Applying acoustic energy directly to the converging channel can cause increased vibrational amplitudes in that area. It is noticeable that the Y-axis exhibits the largest vibration amplitude at a Vpp of 0.50 V, which is significantly different from the Z-axis at the same Vpp by 91.2%. It was discovered that the vertical direction of the Z-axis in the converging channel is lower compared to the region where the acoustic wave flows directly horizontally. Although the vibration data on the Z-axis within this area appears to be less than the Y-axis, these data are mainly similar to the vibration condition obtained at the resonator body on the Z-axis at location point 1, ΔZ1 in Table 3. Nevertheless, the vibration data obtained from the converging channel is still significantly larger than that recorded within the resonator body, with a percentage difference of 17.28% at a Vpp of 0.40 V. Therefore, it is worthwhile to investigate the vibration in both axes of the converging channel, as the data indicates much higher vibrations for all Vpp values compared to the vibration data in Table 3. On the other end, when comparing the vibration data between the converging channel and resonator body, it is noticed that the vibration data on Y-axis for converging channel is higher, while the vibration data for resonator body is higher on Z-axis. The disparity found in this instance can be related to the variation in form and cross-sectional area between these two parts. The converging channel has a larger cross-sectional area than the resonator, while it is smaller in width. Thus, the stiffening and damping characteristics of this part produce different results, with the converging channel being more susceptible to acoustic excitation, particularly along the Y-axis.

3.3.2 Numerical Results

To ensure the identical conditions are replicated in the experimental environment, the numerical analysis has been extended to include the vibrating condition when modelling the acoustic streaming. This study aims to

investigate the impact of vibration on acoustic streaming. The result is as shown in Fig. 7. As previously mentioned during the model validation, the notable disparities between the experimental results and the CFD simulation could be attributed to the fact that the numerical analysis was conducted without accounting for the vibrating effect on the boundary, which is present in the experimental setup. The boundary of the 2D CFD model has been defined according to Fig. 3(b). The simulation includes the principle of moving walls by implementing a dynamic mesh on the top and bottom walls of the model. In this numerical analysis, the top and bottom boundaries of the boundary are modelled to have the same vibrating condition in the Z-axis, similar to the experimental setup. The simulation study primarily addresses the boundary condition within the resonator area. This work will involve the coding of user-defined-function (UDF) and calculation in Eq. 7. The results of this case then will be compared with the first model, without moving wall in terms of flow velocity at highest drive ratio of 3.01%.

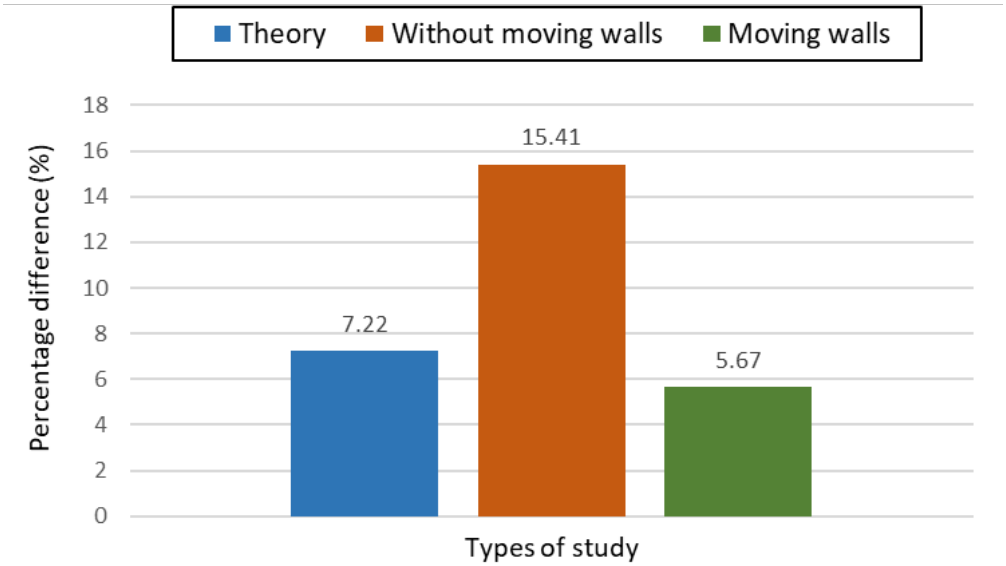

Fig. 7 *Bar chart in comparing the percentage difference between each case and experimental results*

For further analysis, the vibration data obtained throughout the experimental work are utilized in the calculation described by Equation 7 to observe the velocity of the flow streaming. After approximately six cycles, both cases of without moving wall and moving wall is being compared. It can be observed that the flow velocity at the middle point of location 2 for case with moving walls is 1.19% higher than the case without moving walls. The reason for this result lies in the fact that the presence of moving walls leads to a slightly greater maximum velocity. This is due to the boundary condition that captures the dynamic fluid-structure interaction caused by the movement of the wall. This interaction has the potential to result in complex fluid dynamics and increased simulated flow velocities. This finding demonstrates that the vibrating condition has a significant influence on the flow streaming, resulting in an increase in flow velocity. Other than that, the data which is obtained from both cases is also compared with the experimental results. Fig. **7** displayed a bar chart that compares the percentage difference for each case compared to the experimental result. Based on the calculation made, the implementation of moving walls results in a small percentage difference of 5.67% compared to the experimental result. In contrast, the case without moving walls has a percentage difference of 15.41%. This result suggests that implementing moving walls will provide data with more precision, closely resembling the actual situation.

4. Conclusion

The acoustic streaming in an oscillatory flow with the inclusion of vibrating effect was reported based on results obtained from an experimentally validated numerical model. The presence of vibration on the thermoacoustic test rig was detected based on the results obtained from the experimental works. This work provided velocity amplitude data with the presence of vibrating condition for the purpose of model validation. A good match was found for the case with moving walls, while small percentage differences of velocity change with the change of drive ratio was observed between experimental results and CFD simulation for flow frequency of 23.6Hz. This is based on the velocity amplitude plotted in the computational domain representing the location of thermoacoustic rig within the 'stack' area. This proved that the simulation work for case with moving walls to mimic the vibration effect provides the closest scenario to the actual condition as observed in the experiment. The vibrating effects within the converging channel connecting the acoustic driver and the resonator was observed to be larger and further investigation may be needed to understand this impact on the thermoacoustic flow condition.

Nevertheless, the preliminary results presented in this paper through experimental and numerical works indicate that the inclusion of vibration condition into the model lowers the disparity between experimental and numerical results by almost 10%. Hence, its effect on the acoustic streaming and fluid behavior needs further investigation and more data needs to be gathered to better understand this situation. Comprehending vibrations in thermoacoustic systems is crucial due to their significant influence on the interaction between fluid and structure, as well as the overall performance of the system. This inquiry contributes to the continuous endeavors to understand the complex dynamics associated with thermoacoustic flow phenomena.

Acknowledgement

The project is conducted under grant funded by the Ministry of Higher Education Malaysia under FRGS/1/2023/TK08/UTEM/02/1. The authors would like to thank Universiti Teknikal Malaysia Melaka for providing research facilities for this endeavor.

Conflict of Interest

The authors state that none of the work described in this publication appears to have been influenced by any known competing financial interests or relationships.

Author Contribution

The authors confirm contribution to the paper as follows: ***study conception and design****: Nur Afiqah Aina Zaiham, Fatimah Al Zahrah Mohd Saat;* ***data collection:*** *Nur Afiqah Aina Zaiham, Yap Yu Xuan;* ***analysis and interpretation of results****: Nur Afiqah Aina Zaiham, Fatimah Al Zahrah Mohd Saat, Fadhilah Shikh Anuar;* ***draft manuscript preparation:*** *Nur Afiqan Aina Zaiham, Fatimah Al Zahrah Mohd Saat, Patcharin Saechan. All authors reviewed the results and approved the final version of the manuscript.*

References

[1] M. Mahdaoui, S. Kouidri, R. Bennacer, N. Martaj, and M. M. Ali (2015) Energy efficiency of thermoacoustic systems - Study of acoustic streaming in standing wave resonator, in Proceedings of 2015 IEEE International Renewable and Sustainable Energy Conference, IRSEC 2015, Institute of Electrical and Electronics Engineers, https://ieeexplore.ieee.org/document/7455069

[2] H. Bailliet, V. Gusev, R. Raspet, and R. A. Hiller (2001) Acoustic streaming in closed thermoacoustic devices, Journal of the Acoustical Society of America, 110(4), 1808-1821, https://doi.org/10.1121/1.1394739

[3] V. Daru, C. Weisman, D. Baltean-Carlès, I. Reyt, and H. Bailliet (2017) Inertial effects on acoustic Rayleigh streaming flow: Transient and established regimes, Wave Motion, 74, 1-17, https://doi.org/10.1016/j.wavemoti.2017.06.001

[4] P. K. Das, A. D. Snider, and V. R. Bhethanabotla (2020) Acoustic streaming in second-order fluids, Physics of Fluids, 32(12), https://doi.org/10.1063/5.0029229

[5] J. Wu (2018) Acoustic streaming and its applications, Fluids, 3(4), 108, https://doi.org/10.3390/fluids3040108

[6] V. Daru, D. Baltean-Carlès, C. Weisman, P. Debesse, and G. Gandikota (2013) Two-dimensional numerical simulations of nonlinear acoustic streaming in standing waves, Wave Motion, 50(5), 955-963, https://doi.org/10.1016/j.wavemoti.2013.03.004

[7] Y. Yang, G. Jiang, Y. Liu, and Y. Yang (2023) Flow field characteristics of Rayleigh streaming in a two-dimensional rectangular channel under the background physical field, International Communications in Heat and Mass Transfer, 142, https://doi.org/10.1016/j.icheatmasstransfer.2023.106643

[8] J. Lei, P. Glynne-Jones, and M. Hill (2017) Comparing methods for the modelling of boundary-driven streaming in acoustofluidic devices, Microfluidics and Nanofluidics, 21(2), https://doi.org/10.1007/s10404-017-1865-z

[9] Kolesnik, K., Hashemzadeh, P., Peng, D., Stamp, M., Tong, W., Rajagopal, V., Miansari, M., & Collins, D. (2021) Periodic Rayleigh streaming vortices and Eckart flow arising from traveling-wave-based diffractive acoustic fields, *Physical Review, 104(4)*, https://doi.org/10.1103/physreve.104.045104

[10] D. A. Gubaidullin, P. P. Osipov, and R. R. Nasyrov (2014) Numerical simulation of Schlichting streaming induced by standing wave in rectangular enclosure, Journal of Physics: Conference Series, 567, 012017, https://doi.org/10.1088/1742-6596/567/1/012017

[11] S. Moreau, H. Baillet, and J.-C. Valière (2008) Effect of an obstacle on Rayleigh acoustic streaming cells, Journal of the Acoustical Society of America, 123, 3708, https://doi.org/10.1121/1.2935134

[12] R. A. Starr (2001) The effect of streaming on thermoacoustic system, http://researchspace.auckland.ac.nz/

[13] I. V. Egorov, A. V. Fedorov, and N. V. Palchekovskaya (2024) Numerical simulation of laminar-turbulent transition in a supersonic boundary layer under the action of acoustic disturbances, International Journal of Heat and Mass Transfer, 220, 124895, https://doi.org/10.1016/j.ijheatmasstransfer.2023.124895
[14] Y. Zhang, C. Wang, X. Liu, and D. Che (2019) Numerical study of the self-excited thermoacoustic vibrations occurring in combustion system, Applied Thermal Engineering, 160, 113994, https://doi.org/10.1016/j.applthermaleng.2019.113994
[15] A. Jamadin, S. A. Kudus, A. D. H. Ya'akob, M. F. Misnan, and Z. M. Jaini (2023) Vibration-Based finite element model analysis on dynamic characteristics of Ultra-High Performance Concrete beam, International Journal of Integrated Engineering, 15(7), https://doi.org/10.30880/ijie.2023.15.07.020
[16] T. Seshaiah, A. Kumar, S. Shabeer Ali, and D. Rajendra (2022) Experimental investigation of the performance of a thermoacoustic refrigeration, Materials Today: Proceedings, 56(1), 563–567, https://doi.org/10.1016/j.matpr.2022.02.356
[17] M. K. Aktas and B. Farouk (2004) Numerical simulation of acoustic streaming generated by finite-amplitude resonant oscillations in an enclosure, Journal of the Acoustical Society of America, 116(5), 2822–2831, https://doi.org/10.1121/1.1795332
[18] M. Nouh, O. Aldraihem, and A. Baz (2014) Piezo-driven thermoacoustic refrigerators with dynamic magnifiers, Applied Acoustics, 83, 86–99 https://doi.org/10.1016/j.apacoust.2014.02.017
[19] V. Daru, C. Weisman, D. Baltean-Carlès, and H. Bailliet (2021) Acoustically induced thermal effects on Rayleigh streaming, J Fluid Mech, 911, https://doi.org/10.1017/jfm.2020.996
[20] F. A. Z. Mohd Saat, D. Johari, and E. Mattokit (2020) DeltaE Modelling and Experimental Study of a Standing Wave Thermoacoustic Test Rig, Journal of Advanced Research in Fluid Mechanics and Thermal Sciences Journal homepage, 60(2), 155–165, https://akademiabaru.com/submit/index.php/arfmts/article/view/2640
[21] F. A. Z. Mohd Saat and A. J. Jaworski (2017) Numerical Predictions of Early-Stage Turbulence in Oscillatory Flow across Parallel-Plate Heat Exchangers of a Thermoacoustic System, Applied Sciences, 7(7), 673, https://doi.org/10.3390/app7070673
[22] E. Sarpero, E. Gourdon, and D. Borelli (2023) Experimental development and optimization of a standing wave thermoacoustic refrigerator using additive manufactured stacks, International Journal of Refrigeration, 146, 63–73, https://doi.org/10.1016/j.ijrefrig.2022.10.007
[23] J. Kajurek and A. Rusowicz (2020) Experimental investigation on the thermoacoustic effect in easily accessible porous materials, Energies, 14(1), 83, https://doi.org/10.3390/en14010083
[24] N. D. A. Rosle, F. A. Z. Mohd Saat, R.N.F.K. Raja Othman, M.F. Sukri, and P. Saechan (2022) The Effect of Porous Materials on Temperature Drop in a Standing Wave Thermoacoustic Cooler, International Journal of Nanoelectronics and Materials, 15, 405-414, http://dspace.unimap.edu.my:80/xmlui/handle/123456789/76085
[25] O. Olalekan Alabi (2011) Fluid flow in homogeneous and heterogeneous porous media, Electronic Journal of Geotechnical Engineering, 16, 61-70, https://www.researchgate.net/publication/267788911
[26] A. Amirin, T. Triyono, and M. Yulianto (2019) Experimental study of thermoacoustic cooling with parallel-plate stack in different distances, IOP Conference Series: Materials Science and Engineering, 539, 012037, https://doi.org/10.1088/1757-899x/539/1/012037
[27] N. M. Hariharan, P. Sivashanmugam, and S. Kasthurirengan (2012) Influence of stack geometry and resonator length on the performance of thermoacoustic engine, Applied Acoustics, 73(10), 1052–1058, https://doi.org/10.1016/j.apacoust.2012.05.003
[28] P. S. Bhansali, Patunkar P.P, Gorade S.V, Adhav S.S, and Botre S.S (2015) An Overview of Stack Design for A Thermoacoustic Refrigerator, International Journal of Research in Engineering and Technology, 4(6), http://www.ijret.org
[29] S. Putselyk (2019) Measurements of pressure oscillations and mechanical vibrations, IOP Conference Series: Materials Science and Engineering, 502, 012167, https://doi.org/10.1088/1757-899x/502/1/012167
[30] P. Bichkar, O. Dandgaval, P. Dalvi, R. Godase, and T. Dey (2018) Study of Shell and Tube Heat Exchanger with the Effect of Types of Baffles, Procedia Manufacturing, 20, 195–200, https://doi.org/10.1016/j.promfg.2018.02.028
[31] M. A. M. Mohd Dali, R. Abdul Rashid, I. A. Ishak, Z. Mohd Salleh, R. H. Madon, M. Z. Ishak, and N. A. Samiran (2023) CFD Simulation of Air-Piloted Downdraft gasification Process: A comparative study between coal and palm kernel shell as feedstock, International Journal of Integrated Engineering, 15(4), https://doi.org/10.30880/ijie.2023.15.04.010
[32] A. M. N. Elmekawy, A. A. Ibrahim, A. M. Shahin, S. Al-Ali, and G. E. Hassan (2021) Performance enhancement for tube bank staggered configuration heat exchanger – CFD Study, Chemical Engineering and Processing - Process Intensification, 164, 108392, https://doi.org/10.1016/j.cep.2021.108392

[33] D. Feldmann and C. Wagner (2016) On the influence of computational domain length on turbulence in oscillatory pipe flow, International Journal of Heat and Fluid Flow, 61, 229–244, https://doi.org/10.1016/j.ijheatfluidflow.2016.09.005
[34] F. A. Z. Mohd Saat, S. Hajar, A. Mustaffa, and F. Shikh Anuar (2019) Numerical and Experimental Investigations of the Oscillatory Flow Inside Standing Wave Thermoacoustic System at Two Different Flow Frequencies, CFD Letters, 11(8), 1–15, http://eprints.utem.edu.my/id/eprint/24790
[35] M. N. H. Mat, M. F. Azman, and E. M. Yusup (2023) Effect of airborne pathogen transmission released by an assailant in a mosque using CFD simulation. International Journal of Integrated Engineering, 14(4), https://doi.org/10.30880/ijie.2023.15.04.012
[36] M. H. Bagherinejad and R. Kamgar (2020) Improvement of the results of finite element method in plate analysis using mesh sizing modifying function, International Journal of Integrated Engineering, 12(8), 31-43, https://doi.org/10.30880/ijie.2020.12.08.004
[37] H. K. Versteeg and W. Malalasekera (2007) An Introduction to Computational Fluid Dynamics, In Pearson (2nd ed.), Pearson Education
[38] M. P. Ismail, I. A. Ishak, N. A. Samiran, A. F. Mohammad, Z. M. Salleh, and N. Darlis (2022) CFD Analysis on the Effect of Vortex Generator on Sedan Car using ANSYS Software, International Journal of Integrated Engineering, 14(1), https://doi.org/10.30880/ijie.2022.14.01.008
[39] W. Jiang, K. Song, B. Zheng, Y. Xu, and R. Fang (2020) Study on Fast Cold Start-Up method of proton exchange membrane fuel cell based on electric heating technology, Energies, 13(17), 4456, https://doi.org/10.3390/en13174456
[40] S.R. Saiful Azam, S. F. Zainal Abidin, I. A. Ishak, A. Khalid, N. Mustaffa, I. Taib, S. L. Sukiman, N. Darlis (2023) Flow Analysis of Intake Manifold Using Computational Fluid Dynamics, International Journal of Integrated Engineering, 15(1), 88–95, https://doi.org/10.30880/ijie.2023.15.01.008
[41] W. Almukhtar Allafi, F. A. Z. Mohd Saat, and X. Mao (2021) Fluid dynamics of oscillatory flow across parallel-plates in standing-wave thermoacoustic system with two different operation frequencies, Engineering Science and Technology, an International Journal, 24(1), 41–49, https://doi.org/10.1016/j.jestch.2020.12.008
[42] T. D. Rossing and N. H. Fletcher (2004) Principles of Vibration and Sound, Springer (2nd ed.)
[43] E. Leinov, M. J. S. Lowe, and P. Cawley (2015) Investigation of guided wave propagation and attenuation in pipe buried in sand, Journal of Sound and Vibration, 347, 96–114, https://doi.org/10.1016/j.jsv.2015.02.036